Table of contents

Identification of a soft matrix-hard inclusion material by indentation

Tran H. S.[a], Bouffioux C.[a], Dedry O.[b], Rojas-Ulloa C.[a], Duchêne L.[a], Mertens A.[b], Habraken A. M.[a]

[a]*Urban and Environmental Engineering, Materials and Solid Mechanics, University of Liège, Quartier Polytech 1, Allée de la Découverte 9 (B52), B-4000 Liège, Belgium.*

[b]*Aerospace and Mechanical Engineering, Metallic Materials Science, University of Liège, Quartier Polytech 1, Allée de la Découverte 9 (B52), B-4000 Liège, Belgium.*

Abstract

A new procedure for identifying the mechanical behavior of individual phases within a bi-material (matrix-particles) is presented. The case of AlSi10Mg (large globularized Si-rich particles surrounded by an α-Al phase) processed by additive manufacturing and post-treated is taken as a typical example. Grids of nano-indentation tests are performed at different locations on the nanocomposite using a Berkovich indenter and show an impact of the hard inclusions on the experimental curves. The elastoplastic properties of the matrix are identified based on the lowest load–indentation depth curves. Several representative finite element (FE) models demonstrate the influence of the particles on the nano-indentation response. The capacity of the FE model to predict the indentation curve of a cube corner indenter experiment and the Berkovich grid result scattering was checked. A representative volume element (RVE) based on a scanning electron microscope (SEM) image is defined. The identified material parameters of the α-Al phase and Si phase, it allows the prediction of the stress-strain curve of a macroscopic experimental tensile test.

Keywords: AlSi10Mg, nano-indentation, metal matrix composites (MMC), finite element simulation

Corresponding author: hstran@uliege.be (Tran H.S.).

Highlights (364 characters space included)

- Identification of matrix and inclusion behaviors based on nano-indentation grids
- A new set of material parameters for the α-Al matrix
- Data validation by the scattering of Berkovich curves and a cube corner experiment
- Model of post-processed laser powder bed fusion microstructure
- Validation of an RVE model by the simulation of an experimental tensile test

1. Introduction

In mechanical finite element (FE) simulations, the design of a representative volume element (RVE) of a material requires many choices: 2D or 3D model, its size, how the real microstructure is expressed within the mesh (phase distribution, interface behavior, mechanical properties of each phase). This article defines a methodology to determine an accurate RVE for a material microstructure consisting of a soft matrix and hard globular particles. The case of AlSi10Mg samples manufactured by a laser powder bed fusion (LPBF) process and post treated by friction stir processing (FSP) is selected as an application of the method. The research is part of the Longlife AM Walloon Region project whose objective is the numerical identification of the ideal microstructure with improved fatigue properties. This long term objective already requires the design of an RVE able to provide accurate predictions of the local stress and strain fields for a static case. The methodology to identify a simple 2D RVE model is described in this paper.

The multiscale finite element method (MSFEM) and more specifically the RVE approach [1–4] have proven to be highly effective in predicting the behavior of materials with complex microstructures. Usually, computational homogenization is used to estimate the material behavior at the macroscale level. The RVE associated with a 'representative' microstructure is loaded and generates a response able to predict the macroscopic behavior within concurrent simulations or sequential approaches [1]. These results show that the mechanical properties of particle reinforced metals (hereafter called composites, as they consist of a matrix and globular particles), i.e., ductility, fatigue resistance, and wear, depend on the microstructure parameters such as particle size, volume fraction, and distribution, as well as on the particle and matrix behaviors [2–4].

The target application, a LPBF AlSi10Mg sample after FSP, was experimentally characterized by Zhao et al. [5], who compared its microstructure with the one of a LPBF sample heat treated at 300 °C for 2 h. These authors observed that a higher ductility could be achieved by the particle distribution generated by the FSP post-treatment (smaller hard particles and more homogeneous arrangement) compared to a thermal post-treated microstructure. Kim et al. [6] reported that the Si-rich phase controls the damage behavior, as strain localization and incompatibility occur at the Al/Si phase interface. The cracks

mainly occur and propagate in the soft Al matrix. These experimental studies confirm that this material provides an interesting case to apply MSFEM, as the microstructure has a clear impact already on static loading. However, outside the particle size and distribution, an RVE cannot be defined without an accurate procedure to identify the behavior of each phase of the microstructure. The different methods usually used to reach this objective are outlined hereafter.

Classic macroscopic mechanical experiments such as uniaxial or biaxial tensile, compression, shear tests with standardized dimensions provide the average behavior, while indentation tests are recommended to identify more local properties. The indentation technique has attracted the attention of many researchers in recent years [7–9]. For example, automated ball indentation [7,8] and spherical indentation [9–11] provide reasonable indications on the elasto-plastic properties of materials at the macroscale level (millimeter size). However, they do not focus on the elastoplasticity of the individual phases, whereas the nano-indentation test using various indenter shapes has become one of the most common techniques to evaluate the mechanical characteristics of thin films, small bulk samples, and graded materials. It has the advantage of mechanically testing microscale volumes of materials with high accuracy [12–42]. In a composite material, studies [34,36] have proven that experimental data combined with statistical analysis allow for the extraction of the hardness and elastic modulus of each phase. However, the plastic properties of these materials were not considered. For this purpose, a method often used in the literature is the "dimensional analysis", which directly links indentation measurement data to elasto-plastic characteristics. Atkin and Tabor [43–45] first introduced the concept of a representative plastic strain for each indenter shape to interpret cone hardness. From a mathematical viewpoint, they defined complex dimensionless functions that link representative strain and material properties. These non-linear functions are independent of the material strain hardening evolution and must be solved to obtain the elasto-plastic properties. Early studies on "dimensional analysis" were conducted by Cheng and Cheng [46], Dao et al. [47], Ogasawara et al. [48], Bucaille et al. [49], and Tho et al. [50]. The dimensionless functions were calibrated using 2D FE analyses. However, the uniqueness of the solution of plastic flow is only obtained if at least two indenter types are used [51]. Bucaille et al. [41] conducted nano-indentation tests using Berkovich and Cube Corner pyramids on a composite metallic

material consisting of a continuous alumina fiber-reinforced matrix. The stress-strain curves of the matrix were deduced using a reverse procedure. The authors found a good agreement between the flow stress estimated by nano-indentation and uniaxial tests for the material in the cold-worked state, but the discrepancy was large for soft annealed metals. The preliminary work performed by the authors of the present paper using the dimensional analysis on the studied AlSi10Mg alloy confirms this difficulty [23]. Therefore, the inverse modeling method based on FE simulations of the nano-indentation process has been selected as an alternative method [17,22,52–55]. In addition to the identification of the material parameter of each phase, FE simulations of nano-indentation can reveal the local influence of inclusions, while the above dimensional method were limited to the average set of material parameters. However, most numerical studies on nano-indentation have focused on the single-phase or average properties of bulk composites or thin-film behavior. In the present article, the inverse modelling of nano-indentation is applied to the multiphase microstructure of the LPBF AlSi10Mg post-treated by FSP. As pointed out by the literature review hereafter, the parameter identification by nano-indentation of multi-phase materials needs some care, which explains why different model validations were applied in this work.

Recently, Cheng et al. [32] developed an inverse method based on statistical hardness data to identify the elastoplastic parameters of each phase in partitioning and quenching steel. However, the validation of the results with the measured properties obtained by in-situ X-ray diffraction tests was not fully satisfactory. Shen et al. [56,57] studied the correlation between the tensile properties and the hardness of an Al–Cu–Mg alloy reinforced with SiC particles using 2D FE numerical simulations. According to the authors, hardness tests can considerably overestimate the overall tensile and yield strengths of composites with large reinforcing particles. Ekici et al. [58] pointed out that a random small particle distribution and high volume fractions affect the deformed surface profiles, peak indentation force, and local residual stress. Pöhl et al. [59] quantified the influence of the matrix properties on the indentation curve and Young's modulus of an M_7C_3 carbide particle embedded in an X210Cr12 steel matrix using a 2D FE-model. Durst et al. [60] performed 3D FE simulations of nano-indentation to investigate the influence of particles on nickel-based superalloys. Elastic particles embedded in a perfectly plastic matrix were employed to model the particle-matrix composites. They noticed a transitional indentation behavior between the particle and

the matrix, which was also experimentally observed. Duan et al. [61] studied the influence of the distance between the nanoindenter and the fiber on the indentation response of a fiber/matrix composite using a 3D FE simulation. The results revealed that the nano-indentation response strongly depends on the indenter geometry, fiber orientation, and relative distance when the distance is relatively small. Furthermore, the calculated apparent modulus depends on the penetration depth. However, the authors presented only the numerical results without experimental validation, while validated 3D FE simulations of Berkovich nano-indentations carried out on different materials (dental nanocomposites) by Karimzadeh et al. [15] and Heidari et al. [16] confirmed the strong effect of the particle location versus the indenter position. Indeed, when the particle and indenter are close, it generates a stress localization phenomenon that modifies the force-displacement response of the indenter. This literature review demonstrates the need for a careful analysis of the impact of the particle on the nano-indentation results. The described identification methodology of the present article address the distribution and size of the particles as well as the yield stress ratio between the matrix and the particle.

In the literature, two types of constitutive laws are employed in FE simulations of nano-indentation: models based on crystal plasticity [19–21,39,40,52,53,62–64] and macroscopic models [14–18,29–32,54,65–69]. The first approach based on the evolution of the crystallographic texture and dislocation density is widely used to predict the plastic response of polycrystalline materials. However, this approach comes with high experimental uncertainty and requires high computational costs. The second approach, which deals with macroscopic phenomenological models, saves computation time and shows satisfactory accuracy of the results [14,15,17,18,68,70]. Another advantage is to limit the number of parameters to be identified when simple but still reliable phenomenological laws are chosen.

This notion of reliability directly points to the validation method of the predictions of the RVE and of the nano-indentation simulations. The present article gives special care to this validation step, as three comparisons of the measured and computed results are provided: the dispersion ranges of the Berkovich nano-indentation curves, the nano-indentation curve of the matrix deformed by a cube-corner indenter, and a macroscopic tensile test.

2. Experiments

The AlSi10Mg studied material manufactured by LPBF and post-processed by FSP was described by Zhao et al. [5] and Santos Macias et al. [71]. The microstructure showed significant changes between the as-built condition (Fig. 1, a) and after FSP (Fig. 1, b). The FSP significantly improves the material behavior by reducing the LPBF defects, such as porosity and inhomogeneity. The Si particle size after FSP ranged from 10 nm to 690 nm. A more thorough description of the reinforcement particle morphology, size, and distribution can be found in the literature [5,71].

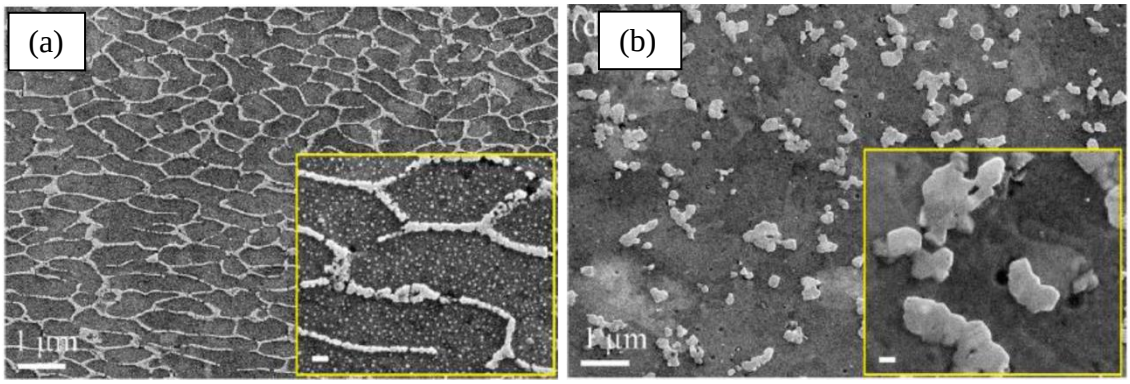

Fig. 1: Scanning electron microscope (SEM) image of the AlSi10Mg material in the as-built state (a) and after FSP post-treatment (b) [5].

The specimen extracted from the FSP zone was polished to a mirror finish. An oxide polishing suspension (OP-S) step was performed for 20 min to reduce the residual stress due to mechanical polishing. The nano-indentation experiment was conducted using a Triboscope Ti950 nanoindenter (Hysitron Inc., USA). A penetration depth of 150 nm was chosen for the Berkovich tip, and the increase and decrease in load were controlled by displacement. The load was increased in 5 s, followed by 5 s holding and 5 s to decrease the load. The indented zone was randomly chosen within the FSP treated zone. A grid of 10 × 10 indentations, separated by 5 µm, was performed. The dispersion of the obtained results was analyzed to reveal the influence of Si nanoparticles. Fig. 2a shows the load-displacement curves of the nano-indentation grid and Fig. 2d shows 3D view of one imprint while Fig. 2b, c enhance the presence of Si particles.

These experimental data show a high dispersion of the loading curves obtained from the indentation grid. It is assumed that the indentation of fine Si particles or of a matrix material involving fine Si particles produces low loading curves, whereas high curves are generated by the indentation involving large Si particles. Section 4 will further confirm this hypothesis through FE simulations.

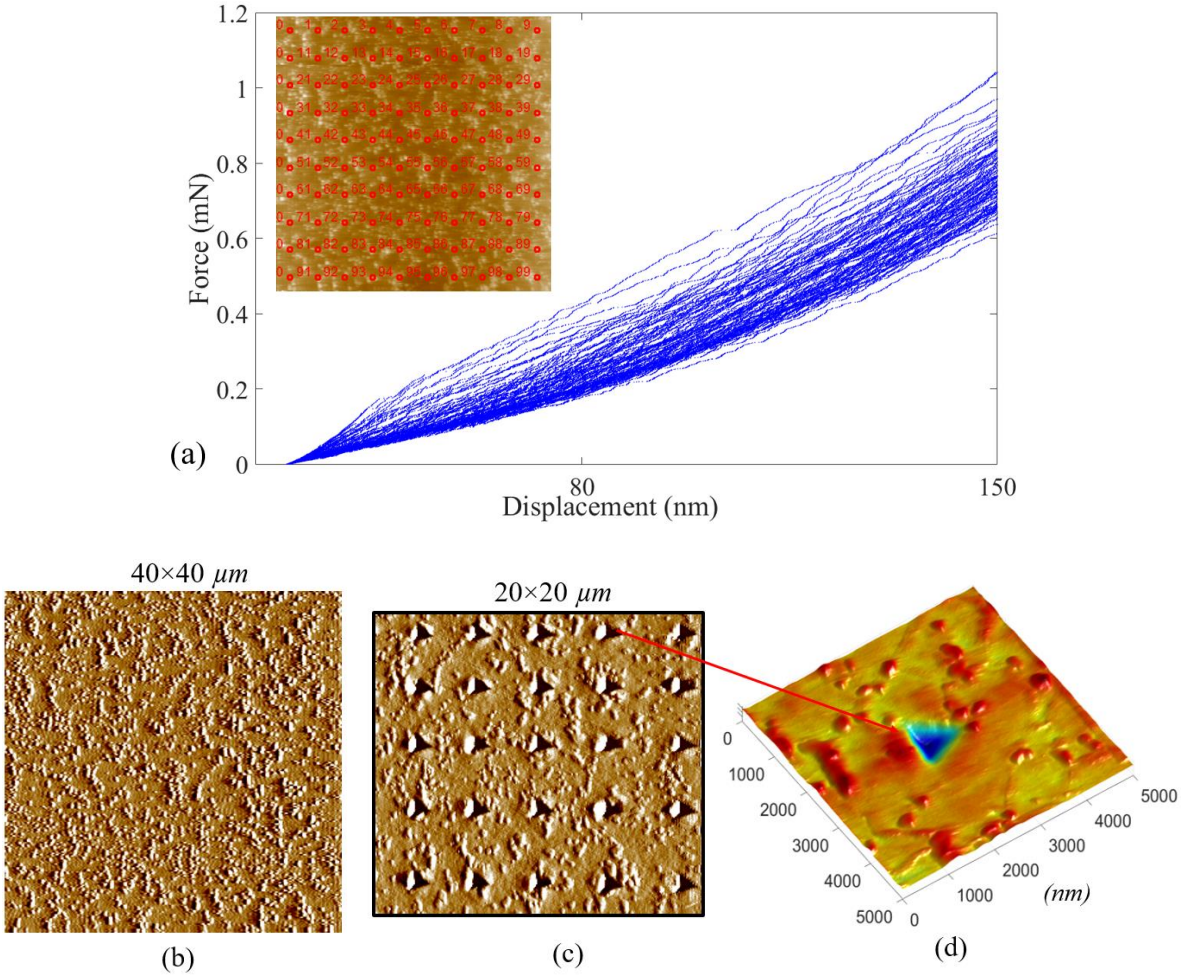

Fig. 2: a) Loading curves of the Berkovich indentation in FSP zones obtained from the grid of nano-indentations of an LPBF - FSP AlSi10Mg sample (from [23]), b) A view of the sample before polishing generated by the scanning mode of the nanoindenter and showing the presence of Si particles, c) a zoom of a part of the 100 nano-indentation grid of the polished sample, d) 3D view of one indent print of the Berkovich indenter in the α-Al matrix of the polished sample.

3. Identification of the mechanical behavior of the Si particle and α-Al matrix

3.1. Si and α-Al elastic parameters

The classical method used to identify the Young's modulus in a single phase material (or neglecting the presence of different phases in the material experimental data post processing) is reminded in this section. The Si data were extracted from one sample where Si particles were larger than in a typical FSP microstructure shown in Fig. 2. The experiments performed in the α-Al matrix within the FSP zone provide the matrix elastic behavior.

The unloading part of the curve of force *F* versus indentation depth *h (F, h)* is assumed to be fully elastic, providing the required information to evaluate the elastic parameters. Sneddon [72] established a link between the slope S at the beginning of this curve, the contact area A projected onto the initial surface of the material, and the reduced modulus E* (Eq. 1).

$$S = \frac{dF}{dh_{h=h_m}} = \frac{2}{\sqrt{\pi}}\, E^* \sqrt{A} \qquad (1)$$

The reduced modulus E^* is defined by Eq. 2, where E, ν and E_i, ν_i represent the Young's modulus and Poisson's ratio of the tested material and the diamond used for the indenter, respectively.

$$\frac{1}{E^*} = \frac{1-\nu^2}{E} + \frac{1-\nu_i^{\,2}}{E_i} \qquad (2)$$

Based on the data available for the related Triboscope system, the diamond values of ν_i and E_i in Eq. (2) are equal to 0.07 and 1140 GPa.

The projection of the contact surface A is defined by Eq. 3:

$$A = C_0 h_c^2 + C_1 h_c + C_2 h_c^{(1/2)} + C_3 h_c^{(1/4)} + C_4 h_c^{(1/8)} + \ldots \qquad (3)$$

where $C_0 = 3.\sqrt{3}.\tan^2\alpha$, α is the centerline-to-face angle, and C_1, C_2, C_3, C_4, … are coefficients that consider small tip defects.

From Eq. 1, the reduced modulus E^* is calculated according to the measured unloading slope S, as follows:

$$E^* = \frac{S}{2}\sqrt{\frac{\pi}{A}} \quad (4)$$

From Eq. 2, the Young's modulus E of the tested material is obtained if its Poisson's ratio is known:

$$E = \left(1-\nu^2\right).\left(\frac{1}{E^*} - \frac{1-\nu_i^{\,2}}{E_i}\right)^{-1} \quad (5)$$

Based on [58,59], the Poisson's ratio of Si particles is assumed to be ν = 0.3, and only the Young's modulus (E_{Si}) is interesting because the elastic limit (approximately 5000 to 9000 MPa) is higher than the local values in the indentation and tensile load case. E_{Si} identification relies on indentations carried out with the Berkovich indenter within the thermo-mechanically affected zone (TMAZ) of the specimens post-processed by FSP. This zone appears at the boundary of the FSP zone (see Fig. 3b and c). The heat generated within the FSP zone affects the TMAZ, which presents no particle cut by the FSP process but a particle growth. These large Si particles are easily indented (average size of 3 μm). For example, the force-displacement curve on such a selected Si particle within the TMAZ is shown in Fig. 3a. The large Si particle size within the TMAZ reduces the influence of the matrix on the Si measurement, as proved by Pöhl et al. [59]. The value obtained by applying the procedure described in hereabove is E = 167 GPa, which is consistent with the literature [73].

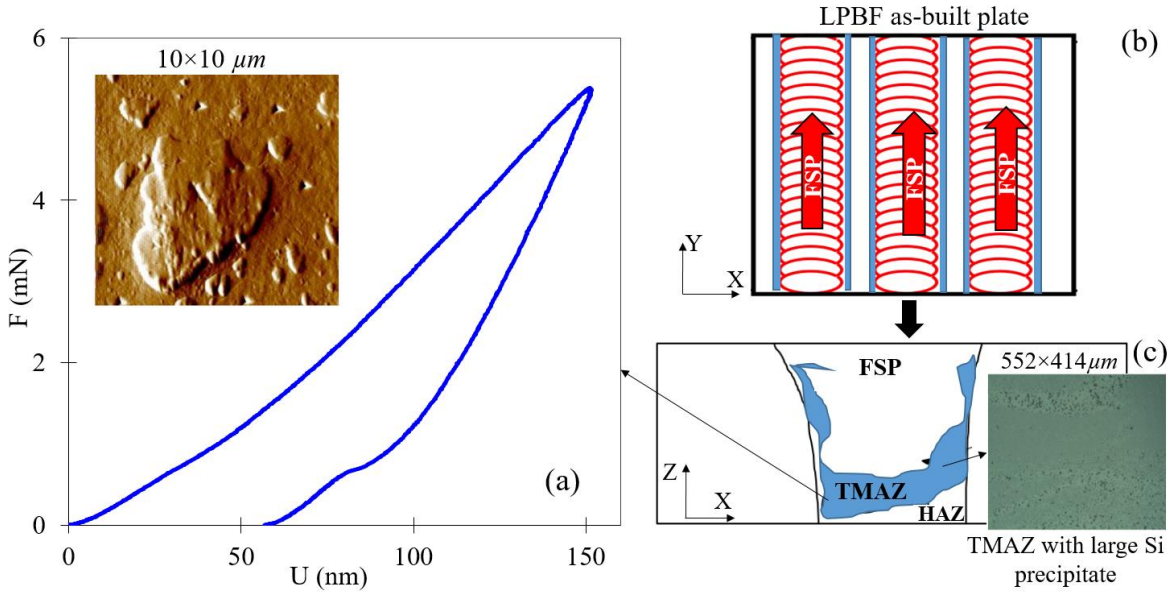

Fig. 3: a) Loading-unloading curve of a Berkovich indentation of a selected Si particle within the thermo-mechanically affected zone (TMAZ) of an LPBF- FSP AlSi10Mg sample, b) scheme of the applied Friction Stir Processing (FSP) post treatment of the plate surface, c) visualization of the FSP post treated zone in the thickness and its surrounding TMAZ.

For the α-Al matrix, the Young's modulus used within this research was obtained based on an initial Berkovich grid indentation campaign [23] performed in 2021 on the post-processed samples (5mm thick) of the AlSi10Mg-FSP material provided by Catholic University of Louvain [5]. This result was compared with the value deduced from the indentation made with the Cube Corner and the value obtained from a macroscopic tensile test. The Young's modulus of the micro elasticity (E = 79.8 GPa) evaluated by the indentations does not fundamentally differ from the one based on the macroscopic tensile test of the composite (E = 71.5 GPa). Note that the results of the FE tensile simulations of a material composed of an elasto-plastic α-Al matrix and elastic Si particles described in section 5.2 also confirm that the Si particles only slightly influence the elastic modulus of the composite. As in [58,59], the Poisson's ratio of the α-Al matrix is assumed to be $\nu = 0.3$.

3.2. Calibration of α-Al Voce hardening parameters with nano-indentation

For the matrix, the relationship between the plastic strain and flow stress is described by the classical isotropic hardening model of the Voce-type as follows:

$$\sigma_F = \sigma_0 + K(1 - \exp(-n.\varepsilon^{pl})) \quad (6)$$

where ε^{pl} is the plastic strain, σ_F is the stress, σ_0 is the yield strength (associated with 0.2% of plastic strain), n is the strain hardening exponent, and K is the material parameter controlling the hardening saturation. In this model, the hardening behavior of the material depends on three unknown constants, K, n, and σ_0.

After the FSP process, the inclusions are randomly distributed Fig. 1b). As a result, the indenter has an arbitrary position in relation to the inclusions when studying the mechanical behavior of the α-Al matrix using an indentation grid. This issue underlines the need for FE simulations to study the effects of the relative position between the particles and the indenter. For simplification purposes, only one inclusion with a spherical shape is discussed hereafter and in the sensitivity analysis of section 4.2.

3D FE simulations of the Berkovich indenter were performed using the Lagamine software developed by the ArGEnCo Department of the University of Liège [20,74]. Taking advantage of the symmetry of the indenter, a half 3D FE model was used to minimize the calculation time. Fig. 4a shows the model size and FE mesh for a representative simulation. The height (6 µm), width (10 µm), and length (5 µm) of the modeled material specimen were sufficiently large compared to the maximum penetration depth of 150 nm to prevent any boundary effect. The smallest element size within the contact area is 25 nm.

The nano-indentation model was meshed using BLZ3D mechanical solid hexahedral elements with a mixed formulation adapted to large displacements and large strains. It employs an hourglass control mechanism and a reduced integration scheme (only one integration point) [75]. Mechanical contact elements [76,77] with four nodes and four integration points were added to model the contact between the specimen and the indenter. The contact was simulated using a penalty algorithm and the Coulomb friction law. A fine mesh was created within the contact region to obtain reliable numerical results. For achieving convergence, the optimal values of the contact penalty coefficient in pressure k_p and the frictional penalty coefficient k_t are $k_p = k_t = 3.7 \times 10^7$ (N/mm^3). Because the Berkovich indenter was significantly stiffer than the specimen, it was modeled as a rigid body.

In these simulations, a typical experimental vertical indenter displacement history was applied at the master node of the indenter along the Y-axis. The maximum displacement (150 nm) was 2.5% of the specimen height. A fixed displacement condition was imposed at the bottom of the FE model, and the horizontal displacement was fixed on the symmetric boundary plane (XY plane). A sensitivity analysis of the friction effect was conducted. It was demonstrated that the effect of the coefficient of friction on the simulation result is negligible, which is consistent with the literature [20,22,61,67,78]. In all simulations, the adopted Coulomb friction value was 0.3.

The results of the nano-indentation experiments were used to calibrate the hardening law of the α-Al matrix of the nanocomposite. The dispersed values of the loading curves associated with the 100 indents of the grid were measured. They reflect the local behavior of the composite instead of the matrix properties, and each curve depends on the relative position of the indenter and the Si precipitates.

Analysis using the scan mode of the nanoindenter (Fig. 2c) and previous numerical studies [15,61] suggest that indentation pressing only on the matrix material yields the lowest force-displacement curve. The target experimental results to identify the α-Al matrix were chosen based on this criterion. The Voce elasto-plastic law parameters were calibrated by manual inverse modeling (minimizing the error between the experimental and predicted force-displacement curve) to obtain numerical indentation results close to the corresponding experimental results. The obtained parameters are shown in Table 1, and the calibrated force-displacement curve shape is physically acceptable Fig. 4b).

Table 1: Calibrated parameters for the α-Al matrix of AlSi10Mg after the FSP

E (GPa) Young's modulus	***ν Poisson's ratio***	***K (MPa)***	***σ_0 (MPa) Yield limit***	***n***
79.8	0.3	180	180	17

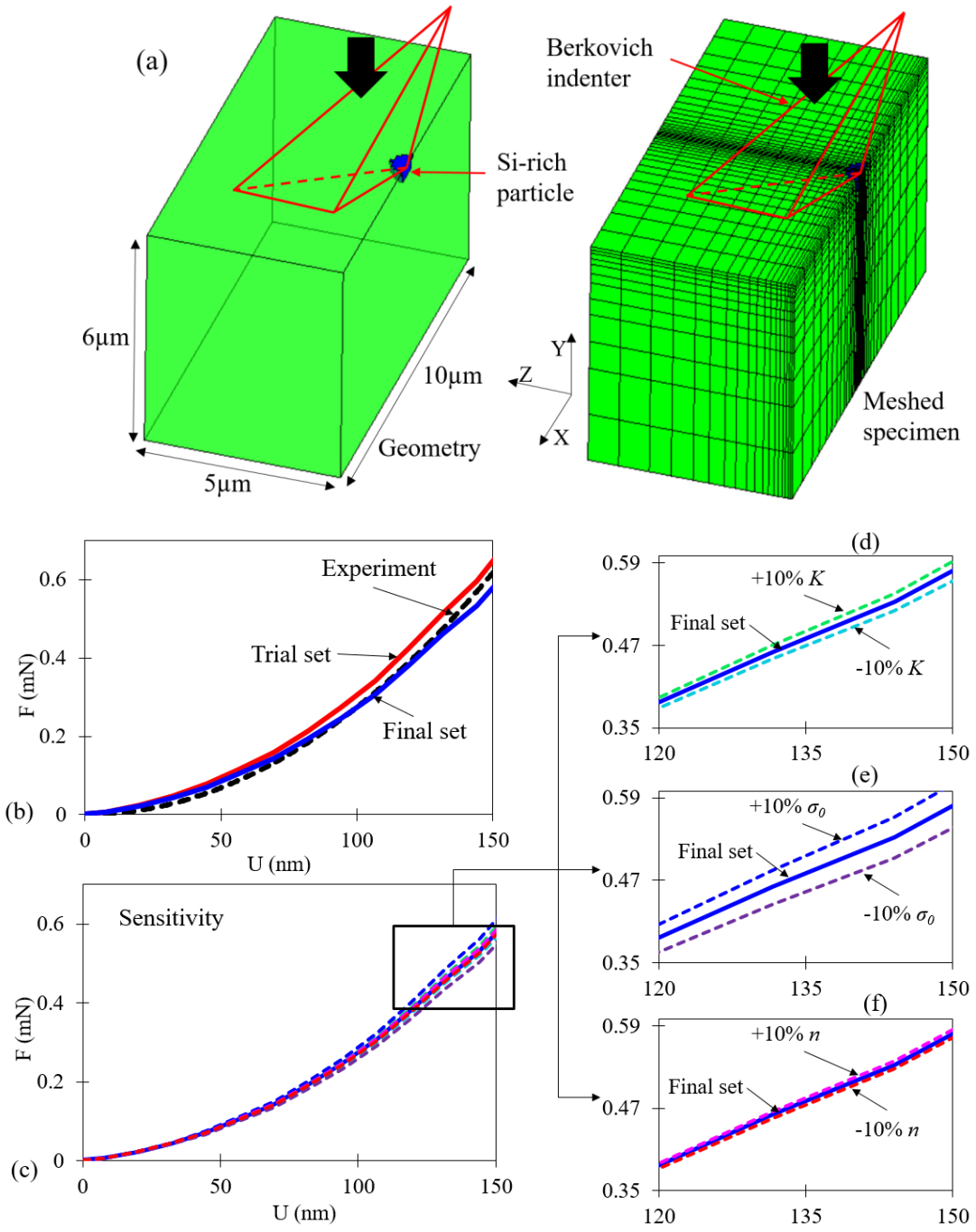

Fig. 4: a) Geometry and FE mesh for the α-Al matrix with one Si-rich inclusion, b) Numerical simulations with the initial and calibrated final data set for the α-Al matrix of a Berkovich nano-indentation and the experimental result of the indentation of the α-Al matrix of an LPBF-FSP AlSi10Mg sample (lower curve of the set of experiments). c, d, e, f) Sensitivity of the computed nano-indentation curves to the parameters of the hardening law of the α-Al matrix compared with the calibrated parameters.

Note that compared to the Voce hardening law results, the Swift hardening model does not provide a better agreement between the predictions and experiments. Perturbing separately, each of the three parameters of the Voce law with the same relative amount of ±10% from their identified values demonstrates their impact on the curve (Fig. 4c, d, e, f). The difference between the reference and sensitivity curves was relatively low until 60 nm but increased with the imposed displacement. A more pronounced effect on the indentation curve is generated by the disturbance of the yield limit σ_0 and parameter K than the function exponent n. It was observed that a ±10% change in σ_0, K, and n leads to a variation of more than ± 5.5%, ± 2.45%, and ± 0.95%, respectively, in the indentation response at an indentation depth of 150 nm. Consequently, to identify the parameters of the hardening law by the Berkovich nanoindenter, the applied displacement should be greater than 60 nm. Multiple solutions could be reached; however, the data set of Table 1 provided a minimal error between the model prediction and the experiment. In section 4, the calibrated set of parameters is used to examine the effect of nanoparticles on the loading response.

4. Impact of particles within indentation results

In section 4.1, FE simulations allow the influence of different inclusion sizes and the relative locations between the inclusion and indentation to be investigated, while section 4.2 analyses the perturbation brought by the Si particle within the local strain field and the plastic volume affected by the indentation.

4.1. Sensitivity analysis related to the inclusion size and the indenter position

Any inclusion is assumed to be perfectly bonded with the matrix, and the largest measured inclusion diameter is D = 690 nm, which defines the limit to explore. The sensitivity result analysis is presented hereafter.

Fig. 5 shows the three representative configurations studied. Note that D, the diameter of the inclusion, varies from 100 nm to 690 nm; h and L are the horizontal and vertical distances between the inclusion and the indentation point, respectively. The ratio h/D is between 0 and 1.5, and L/D evolves between 0 and 1.

Fig. 5a shows the force-displacement curves corresponding to 4 different inclusion diameters. The blue curve shows the response to the matrix material without any inclusion

(Reference case). At the same indentation depth, the influence of the inclusion increases with an increase in its size. For example, when the inclusion size is 690 nm, the force is 50% higher than that without the inclusion when the displacement reaches 150 nm. However, the effect rapidly decreases when the inclusion diameter is smaller than 350 nm, and its influence is negligible when the inclusion diameter is less than 200 nm.

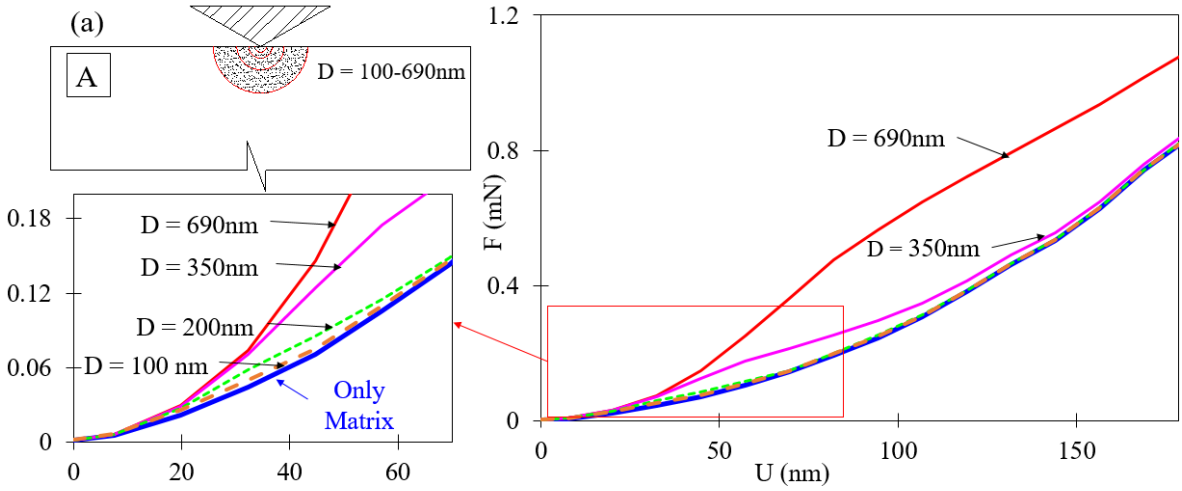

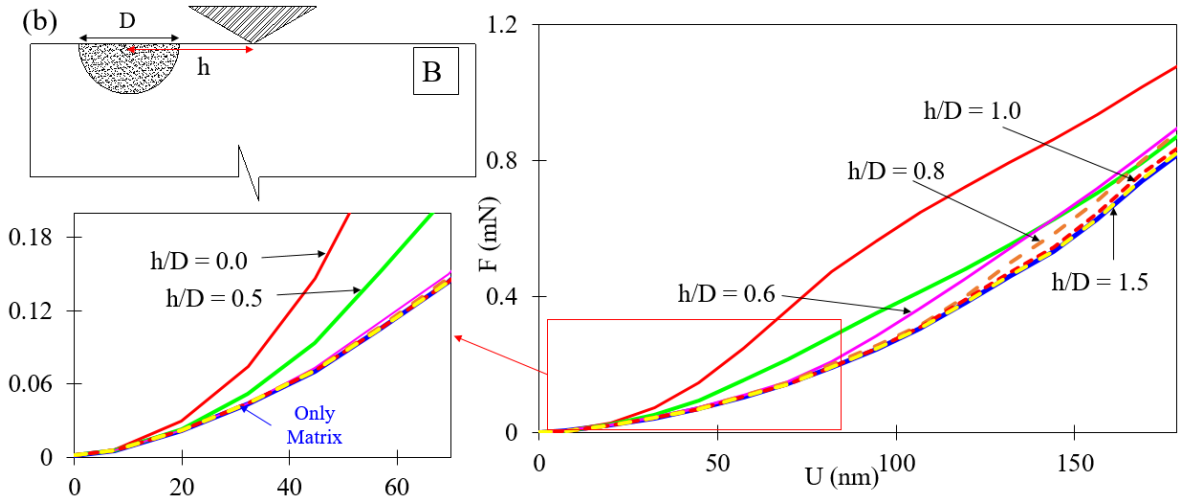

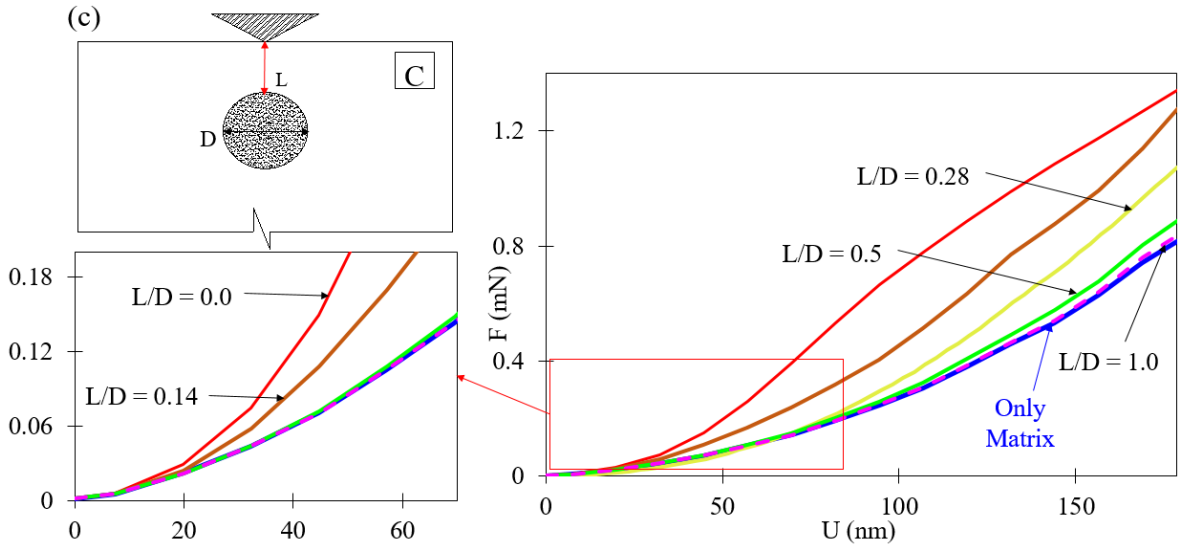

Fig. 5: Simulated nano-indentation cases with an inclusion embedded in the α-Al matrix with different sizes of Si inclusion and different positions between the indenter and inclusion. a) Force-displacement curves for a Berkovich indentation directly applied above half of the inclusion, b) applied with different distances between the inclusion and the indenter (D = 690 nm), c) directly applied above the inclusion (D = 690 nm).

The force-displacement curves in Fig. 5b show the response when indentation occurs in the matrix region. Because of the continuity assumption between the matrix and precipitate, both the Si precipitate and aluminium matrix properties contribute to the result when the interface between the inclusion and the matrix is indented (case B - h/D = 0.5). When the h/D ratio is equal to 0.6 and 0.8, the effect of the inclusion is only clear when the imposed indenter depth reaches approximately 70 nm and 100 nm, respectively. When the ratio was increased to 1, the influence of the inclusion was not observable before 150 nm. This observation implies that for the largest precipitates present in the material, the deformation zone was limited to a distance of less than 345 nm (690/2 nm).

For the vertical inclusion model (Fig. 5c), while L/D is equal to 0, the inclusion is tangent to the surface. For this case, at 150 nm of indentation, the force is 85% higher than the reference case without the inclusion and 22% higher than the case of h/D equal to 0 (half of the inclusion defines the surface). Indeed, the inclusion volume significantly influences the maximum force when the indenter directly touches the inclusion. This influence is negligible if the inclusion diameter is less than 200 nm. As the L/D ratio is increased, the indenter is

placed in the matrix. As shown in Fig. 5c, the inclusion effect decreases when L/D increases. When L/D = 1, the influence of the inclusion is insignificant, indicating that once the displacement is less than a critical distance, the matrix response dominates.

In summary, for this material with a $\frac{\sigma_Y matrix}{\sigma_Y inclusion}$ ratio of 0.036 and Si particle sizes ranging from 100 nm to 690 nm, the 3D FE simulation results show that the force-displacement curve of the Berkovich nanoindenter is not affected if the particle size is smaller than 200 nm. An additional conclusion is that the matrix behavior can be identified by an indent that stays at a distance of 345 nm from the largest inclusions.

4.2. Analysis of equivalent plastic strain and stress fields near the indenter

The von Mises strain contours are plotted to show the strain distribution to further analyze the local behavior beneath the indenter. Fig. 6b, c, and d show the equivalent strain fields associated with an indentation depth of 100 nm and the largest inclusions (690 nm diameter) with an identical maximum scale of 0.06 strain. The plastic volume fraction $V_{Plastic}$ is highly dependent on the relative position between the inclusion and the indenter. The maximum $V_{Plastic}$ corresponds to the reference case without any inclusion Fig. 6a. In addition, the influence of rigid inclusions on the distribution of the plastic strain is observed. When the indenter directly touches the center of the inclusion Fig. 6b, the plastic strain is much lower within the matrix than in the reference case, and it is relatively uniformly distributed. Once the indenter pressed the matrix Fig. 6c and d, the plastic deformation zone rapidly increases, but the presence of inclusions modified the plastic strain distribution.

Fig. 7 presents the contours of the von Mises stress in the α-Al matrix and Si particle at a displacement of 100 nm. It is observed that the materials within the matrix of the four models have stress levels ranging from 200 to 300 MPa. However, Fig. 7b-c shows that the stress in the Si particle is higher than 400 MPa. Thus, particle size and location have a significant effect on the stress distribution. This phenomenon explains the increase in the load-displacement curve of these nano-indentation tests.

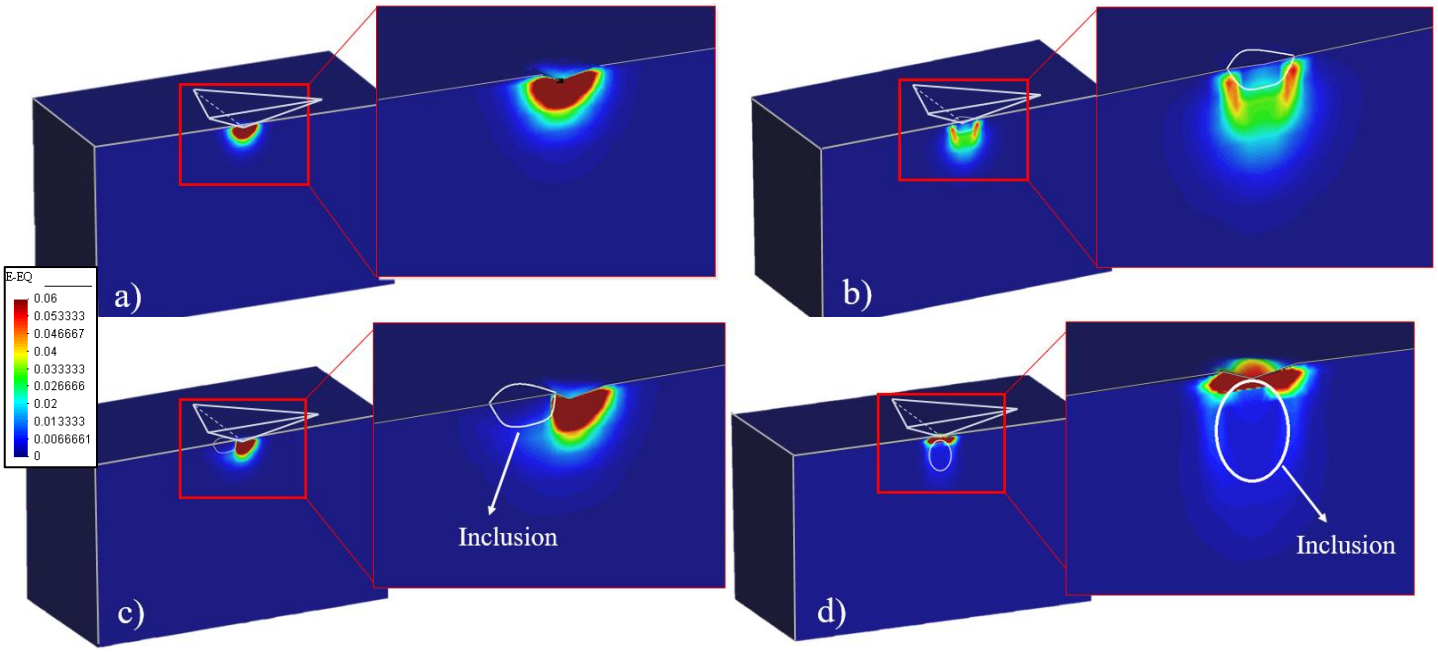

Fig. 6: von Mises strain fields calculated by FE with the Berkovich indenter with an imposed displacement of 100 nm (a) without inclusion, b) with inclusion h/D = 0, (c) h/D = 0.6, (d) L/D = 0.14.

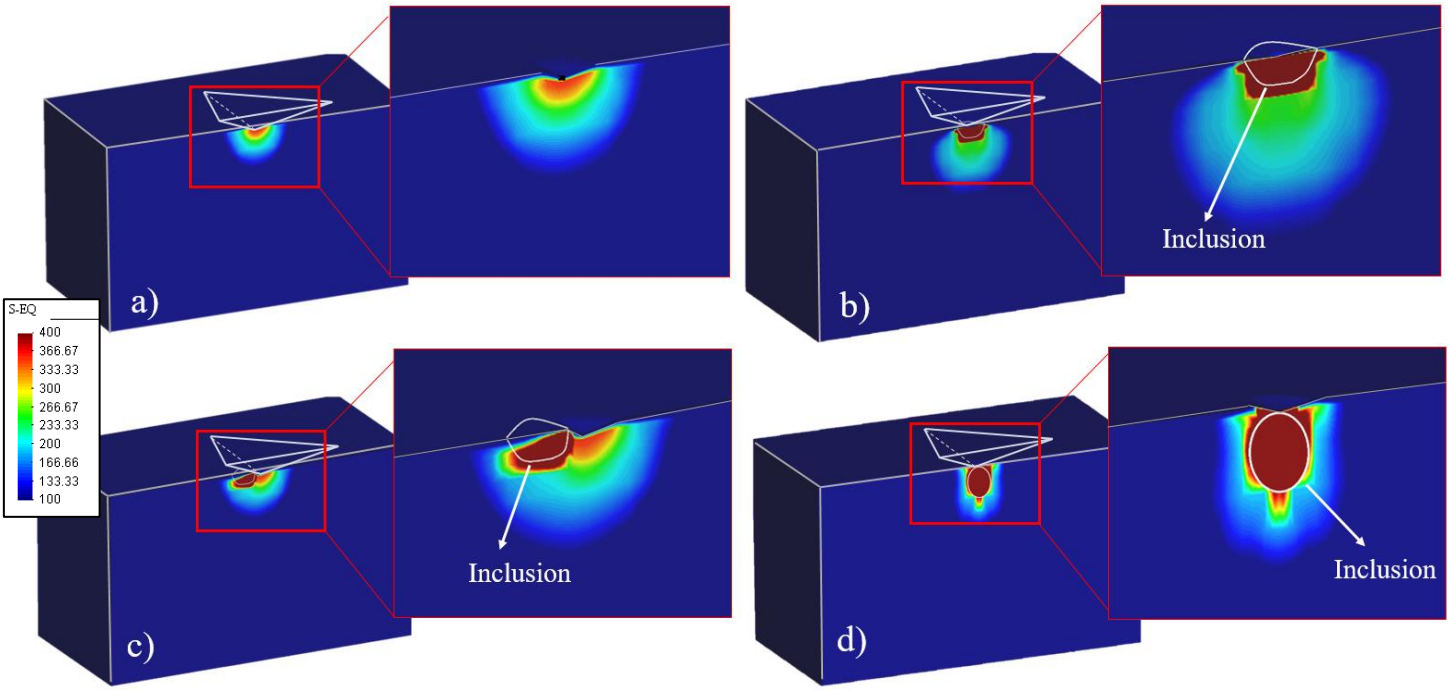

Fig. 7: von Mises stress fields calculated by FE with the Berkovich indenter with an imposed displacement of 100 nm (a) without inclusion, b) with inclusion h/D = 0, (c) h/D = 0.6, (d) L/D = 0.14.

The above analysis proves that force-displacement dispersion as obtained, for instance, in Fig. 2 can be related to the size of the inclusion and its relative position to the indent. Therefore, selecting the representative force-displacement curve is essential for extracting the mechanical properties of each phase in the composite. Matrix identification requires grid measurements to provide multiple curves in case of a matrix and particle microstructure. In this study, 100 curves were obtained and only the lowest ones were used to identify the α-Al behavior.

5. Validations

The identified material data set of Table 1 is checked by the comparisons of the experimental and numerical ranges of the Berkovich indentations of the biphasic material (section 5.1). A second validation is also presented in section 5.1 for the case of the Cube Corner indentation, while an experimental tensile curve and its RVE simulation are described in section 5.2.

5.1. Validation of nano-indentation experiments

Some FE simulation results compared with the force-displacement data measured by the automatic grid indentation tests are shown in Fig. 8a. The variation ranges of the computed force-displacement curves of the composite associated with the values of h/D and L/D defined by the conclusion given in of section 4.1 predict, with an acceptable accuracy, the deviation of the experimental curves (≈ 0.5 mN). This agreement provides the first validation of the FE rheological model. Furthermore, it illustrates the accuracy of the identified plastic curve (both the yield limit and hardening model).

A nano-indentation grid of 10 x 10 indents using a Cube Corner indenter was performed to provide a second validation of the calibrated set of parameters determined by the Berkovich experiments. A penetration depth of 430 nm was chosen to obtain the same contact area as with the Berkovich indenter, and the lowest curve of the grid indentation was selected. Fig. 8b shows a good agreement between the FE simulation and the experiment, confirming the identified set of parameters for the Voce law (Table 1).

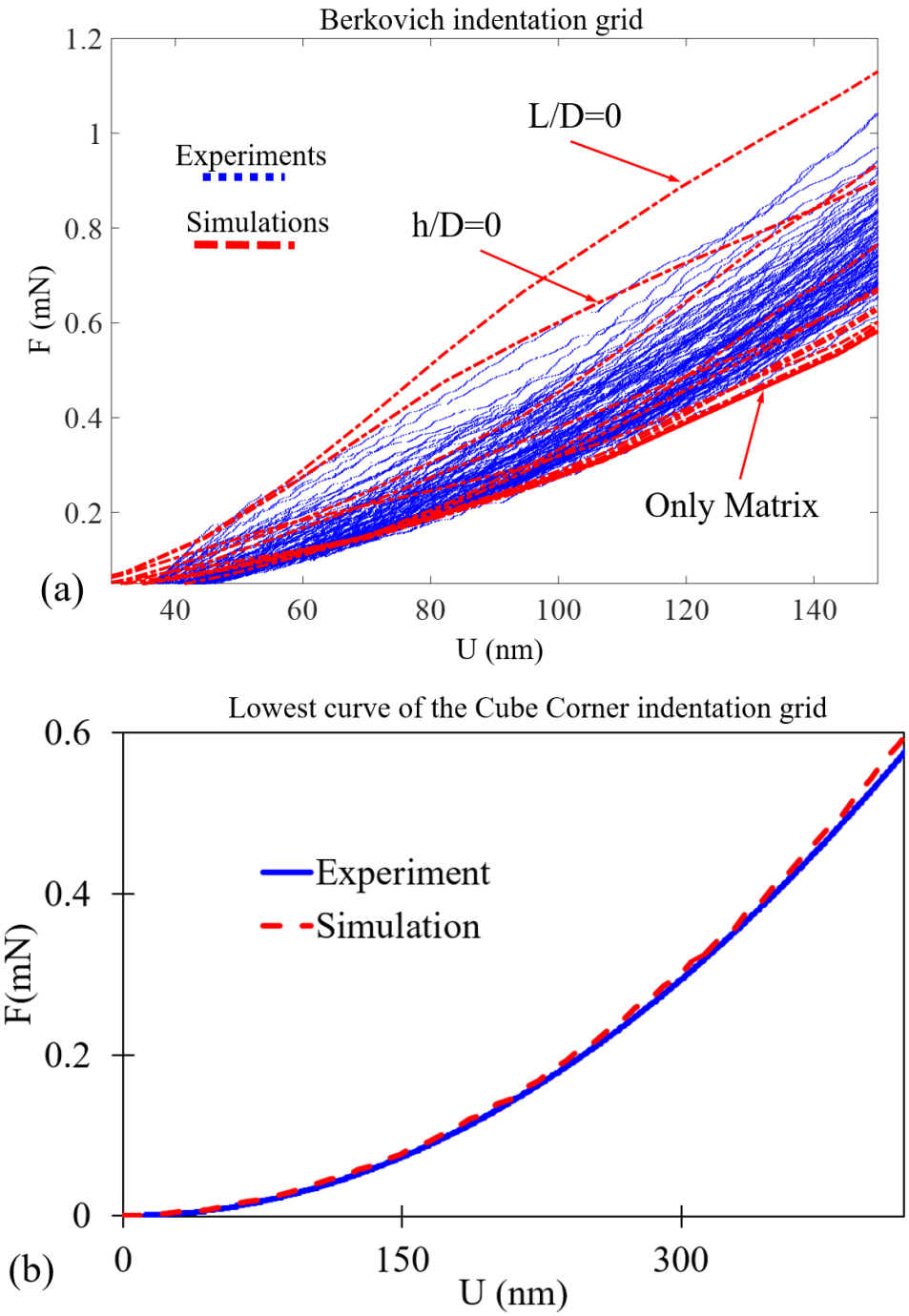

Fig. 8: (a) Dispersion of the Berkovich nano-indentation curves obtained from the FE simulations with various sizes and positions of the Si particles and results of experiments obtained from the nano-indentation grid; (b) Numerical simulation of nano-indentation of Cube Corner indenter inside the α-Al phase without Si particles with the calibrated parameter set in Table 1 and the lowest result of the Cube Corner grid experiments within LPBF-FSP AlSi10Mg sample.

5.2. RVE application for tensile curve prediction

A third validation of the behavior of each phase and of the selected representative inclusion sizes, shapes, and their distribution within the RVE can be achieved by comparing its global behavior with the macroscopic flow stress. Experimentally, a tensile experiment was performed on AlSi10Mg after FSP [5]. First, the initial microstructure was characterized by SEM observation; then, a surface mechanical polishing and etching step with hydrofluoric (HF) (0.5% vol) acid was applied, and finally, a uniaxial tensile test was conducted following the ASTM E8/E8M-15a standard on a Zwick machine with a constant loading rate [5].

From a numerical point of view, a simplified microstructure based on the SEM image in Fig. 9a was used to generate the studied RVE. The image was filtered using ImageJ software, and the morphological Si particles were derived as ellipses. The size of the Si inclusions present in the RVE ranged from 100 to 690 nm. The finite element simulation relies on a volume including 110 Si particles. The large size of the model explains why no periodic conditions were applied. A single layer of BLZ3D elements with a free lateral surface type boundary condition was applied (Equations 7). Due to the 3D constitutive law and the large difference in the strengths of the matrix and inclusion, the mesh size, and boundary conditions, the result is between the plane strain and plane stress state. Note that thickness variations are generated. The accuracy of such an assumption is not perfect, but it is far faster than a full 3D RVE. Note that this simple assumption was also adopted in [79].

$$\begin{cases} U_x\left(0,y,z\right)=0 \\ U_x\left(L,y,z\right)=U_x^* \\ \vec{t}=\sigma\vec{n}=0 \text{ for any lateral faces} \end{cases} \quad (7)$$

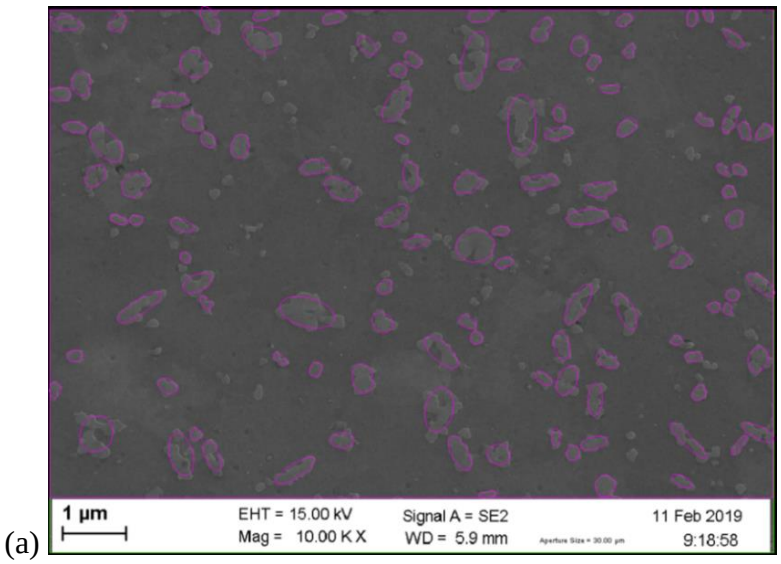

(a)

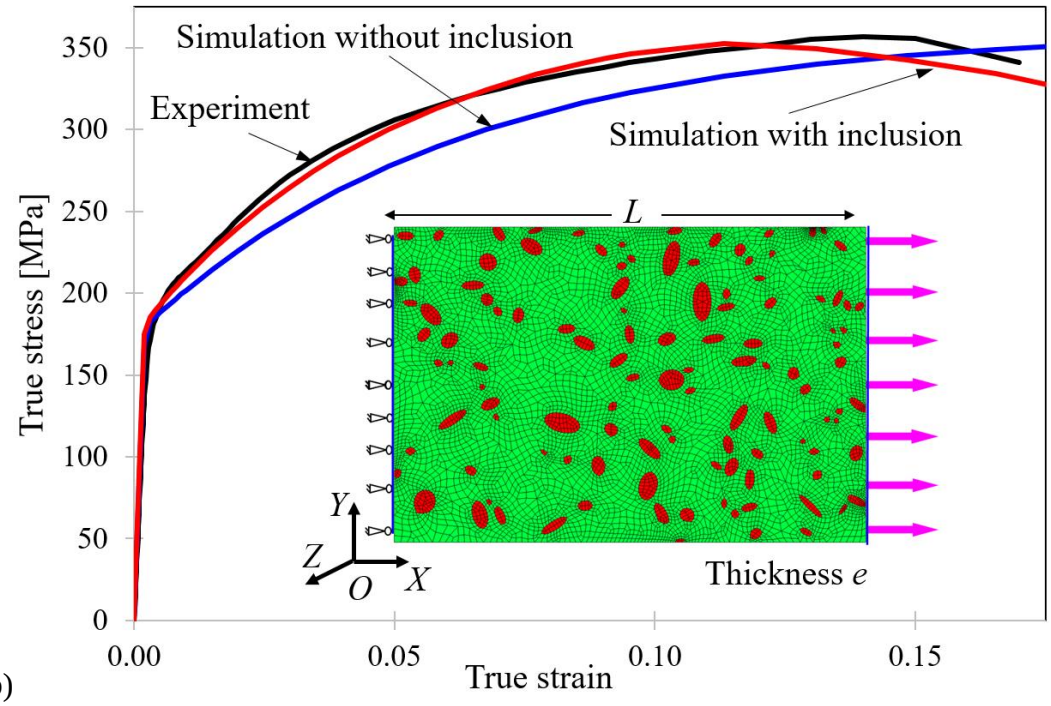

(b)

Fig. 9: a) Microstructure of the LPBF-FSP AlSi10Mg sample [5] used to define the RVE; b) Measured true stress-true strain response of the composite under axial tension and computed by RVE model (RVE mesh with Si particles in red, the α-Al matrix in green, and boundary conditions).

A comparison between the experimental and simulated true stress-true strain curves computed with a similar method ($\sigma=F/A$, $\varepsilon=ln(L/L_0)$) is shown in Fig. 9b. The blue curve results from the model without inclusion (hole instead of inclusion), whereas the red curve is

obtained with elastic inclusions. It can be observed that the effect of the inclusion on the elastic limit and Young's modulus is insignificant. According to this simulation, the matrix properties dominate the elastic behavior of the AlSi10Mg composite after FSP. However, the results show that the inclusions increase the work hardening effect of the material. The computed true stress-true strain curve (red curve) is very close to the experimental value up to 12% macroscopic strain.

The equivalent von Mises strain fields corresponding to two levels of macroscopic deformation 5% and 12% are presented in Fig. 10a and b, respectively. At a macro strain of 5%, the maximum deformation value was two times higher than the average strain, quantifying the high heterogeneity within the matrix. For a macroscopic strain of 12%, the maximum local strain value was three times higher than the average strain with a significant localized band that crossed the specimen. At this level, a stress drop is observed within the FE computed curve with the inclusion in Fig. 9b. Thus, the numerical calculation fails to accurately predict the macroscopic average behavior (stress-strain) in the strain domain above 12%. This bad prediction could probably be avoided if cohesive elements would be implemented between the Si particles and the matrix.

(a)

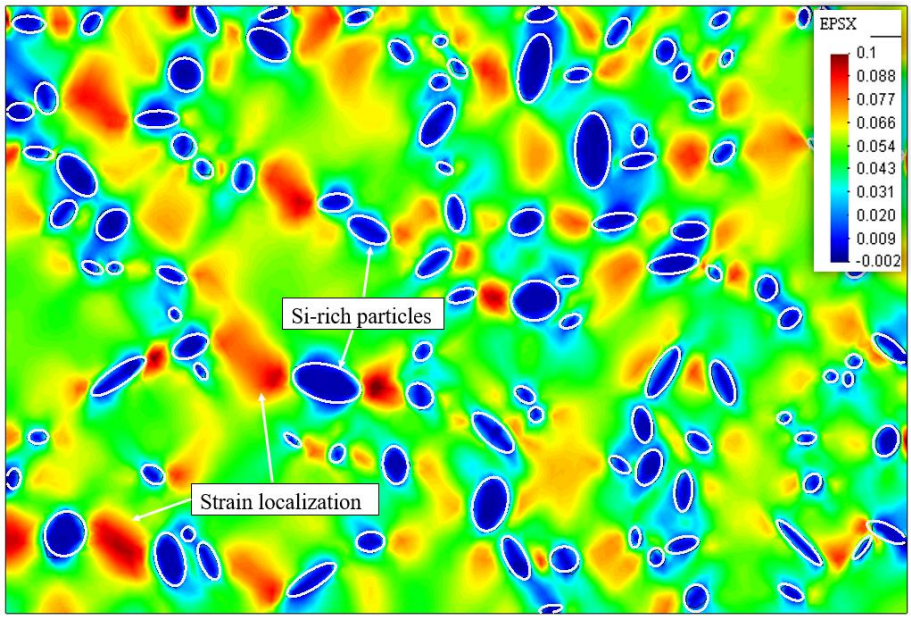

(b) 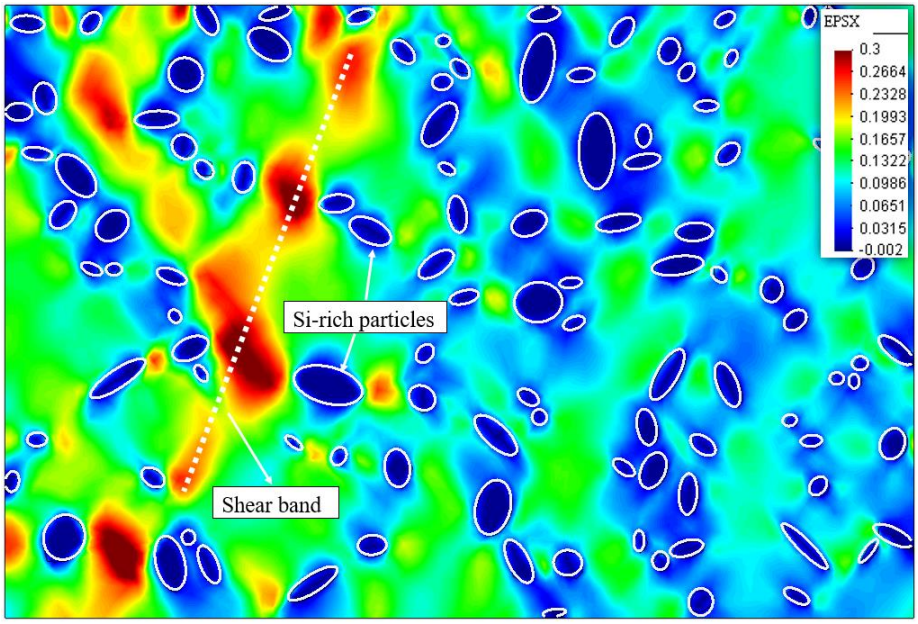

Fig. 10: Distribution of the equivalent local strain at various loading values of macroscopic strain: a) 5%, b) 12%.

Experimentally, Zhao et al. [5] observed decohesion between the matrix and Si particles for strains above 9%. Therefore, predicting the average stress drop will be studied, including a cohesive model in a real 3D RVE [79–82]. Furthermore, an improved RVE smaller but closer to a real 3D bulk structure due to periodic conditions will be used to better model the material state in future research.

6. Conclusions

In this study, an effective identification approach based on grid nano-indentation experiments is developed to extract the elastoplastic behavior of a matrix that contains hard particles. Applied on AlSi10Mg samples generated by the LPBF process with a FSP post-treatment, the method is validated by the developed FE models and their predictions. Three different validations are presented: i) The high dispersion of Berkovich curves due to the presence of Si nanoparticles is correctly predicted; ii) The FE simulation of the loading curve of a cube corner (not used in the identification process) matches well with the experiment; iii) The FE simple RVE based on a SEM image and the identified data set recovers the experimental curves up to 12% strain. For deformations larger than 12%, the tensile strain generates damage at the particle-matrix interface. Therefore, a cohesive zone method should be added

to the FE model. Such an improved approach, as well as the use of real 3D RVE, should improve the representativeness of the RVE. These extensions are mandatory if one wants to use the model to predict the correct damage in phenomena strongly linked to local features like static rupture or fatigue behavior. The authors are working further in this direction, relying on an ongoing experimental campaign of fatigue tests.

This article has demonstrated through FE simulation results how the indentation location related to the hard particle position and the particle size, modifies the force-penetration curve. For the specific case with a soft matrix and high strength particles with a yield limit ratio $\frac{\sigma_Y matrix}{\sigma_Y inclusion}$ of 0.036 and an inclusion size ranging from 100 nm to 690 nm, the results show that : (i) Particles smaller than 200 nm do not affect the force-displacement curve using a Berkovich nanoindenter; (ii) The matrix behavior can be measured by an indentation that stays at a minimum distance of 345 nm from an inclusion.

Acknowledgments

This research was conducted within LongLifeAM project of WALInnov program - Convention 1810016 Région Wallonne. We acknowledge Aude Simar's UCL team for providing FSP samples as the partner of this project. As Research Director of F.R.S-FNRS, AM Habraken acknowledges the support of this institution. Computational resources were provided by the Consortium des Équipements de Calcul Intensif (CÉCI), also funded by the F.R.S.-FNRS, under Grant No. 2.5020.11. CAREM of ULiege is thanked for providing SEM/EDS facilities. C. Rojas-Ulloa acknowledges the international cooperation agreement WBI/AGCID SUB2019/419031 (DIE19-0005) project 06 DommaCo.

References

[1] M.G.D. Geers, V.G. Kouznetsova, W.A.M. Brekelmans, Multi-scale computational homogenization: Trends and challenges, J. Comput. Appl. Math. 234 (2010) 2175–2182. https://doi.org/https://doi.org/10.1016/j.cam.2009.08.077.

[2] H.M. Inglis, P.H. Geubelle, K. Matouš, H. Tan, Y. Huang, Cohesive modeling of dewetting in particulate composites: micromechanics vs. multiscale finite element

analysis, Mech. Mater. 39 (2007) 580–595. https://doi.org/https://doi.org/10.1016/j.mechmat.2006.08.008.

[3] J. Segurado, J. Llorca, A numerical approximation to the elastic properties of sphere-reinforced composites, J. Mech. Phys. Solids. 50 (2002) 2107–2121. https://doi.org/https://doi.org/10.1016/S0022-5096(02)00021-2.

[4] M. Teranishi, O. Kuwazuru, S. Gennai, M. Kobayashi, H. Toda, Three-dimensional stress and strain around real shape Si particles in cast aluminum alloy under cyclic loading, Mater. Sci. Eng. A. 678 (2016) 273–285. https://doi.org/https://doi.org/10.1016/j.msea.2016.10.004.

[5] L. Zhao, J.G. Santos Macías, L. Ding, H. Idrissi, A. Simar, Damage mechanisms in selective laser melted AlSi10Mg under as built and different post-treatment conditions, Mater. Sci. Eng. A. 764 (2019) 138210. https://doi.org/https://doi.org/10.1016/j.msea.2019.138210.

[6] D.-K. Kim, W. Woo, J.-H. Hwang, K. An, S.-H. Choi, Stress partitioning behavior of an AlSi10Mg alloy produced by selective laser melting during tensile deformation using in situ neutron diffraction, J. Alloys Compd. 686 (2016) 281–286. https://doi.org/https://doi.org/10.1016/j.jallcom.2016.06.011.

[7] C. Ortiz Rios, T. Amine, J.W. Newkirk, Tensile behavior in selective laser melting, Int. J. Adv. Manuf. Technol. 96 (2018) 1187–1194. https://doi.org/10.1007/s00170-018-1663-0.

[8] T. Pan, S. Karnati, Y. Zhang, X. Zhang, C.-H. Hung, L. Li, F. Liou, Experiment characterization and formulation estimation of tensile properties for selective laser melting manufactured 304L stainless steel, Mater. Sci. Eng. A. 798 (2020) 140086. https://doi.org/https://doi.org/10.1016/j.msea.2020.140086.

[9] C. Schneider-Maunoury, A. Albayda, O. Bartier, L. Weiss, G. Mauvoisin, X. Hernot, P. Laheurte, On the use of instrumented indentation to characterize the mechanical properties of functionally graded binary alloys manufactured by additive

manufacturing, Mater. Today Commun. 25 (2020) 101451. http://www.sciencedirect.com/science/article/pii/S2352492820324624.

[10] A. Bahri, M. Ellouz, M. Klöcker, T. Kordisch, K. Elleuch, Brinell indentation behavior of the stainless steel X2CrNi18-9: Modeling and experiments, Int. J. Mech. Sci. 163 (2019) 105142. https://doi.org/https://doi.org/10.1016/j.ijmecsci.2019.105142.

[11] Y. Hwang, K.P. Marimuthu, N. Kim, C. Lee, H. Lee, Extracting plastic properties from in-plane displacement data of spherical indentation imprint, Int. J. Mech. Sci. 197 (2021) 106291. https://doi.org/https://doi.org/10.1016/j.ijmecsci.2021.106291.

[12] N.E. Uzan, R. Shneck, O. Yeheskel, N. Frage, Fatigue of AlSi10Mg specimens fabricated by additive manufacturing selective laser melting (AM-SLM), Mater. Sci. Eng. A. 704 (2017) 229–237. http://www.sciencedirect.com/science/article/pii/S0921509317310316.

[13] A.C. Fischer-Cripps, Nanoindentation, Springer, New York, 2002. https://doi.org/10.1007/978-0-387-22462-6.

[14] A. Karimzadeh, M.R. Ayatollahi, M. Alizadeh, Finite element simulation of nano-indentation experiment on aluminum 1100, Comput. Mater. Sci. 81 (2014) 595–600. https://doi.org/https://doi.org/10.1016/j.commatsci.2013.09.019.

[15] A. Karimzadeh, R. Koloor, M.R. Ayatollahi, A.R. Bushroa, M.Y. Yahya, Assessment of nano-indentation method in mechanical characterization of heterogeneous nanocomposite materials using experimental and computational approaches, Sci. Rep. 9 (2019) 15763. https://doi.org/10.1038/s41598-019-51904-4.

[16] M. Heidari, A. Karimzadeh, M.R. Ayatollahi, M.Y. Yahya, Effects of particle distribution and calculation method on results of nano-indentation technique in heterogeneous nanocomposites-experimental and numerical approaches, Int. J. Solids Struct. 225 (2021) 111054. https://doi.org/https://doi.org/10.1016/j.ijsolstr.2021.111054.

[17] C.-M. Sanchez-Camargo, A. Hor, C. Mabru, A robust inverse analysis method for elastoplastic behavior identification using the true geometry modeling of Berkovich indenter, Int. J. Mech. Sci. 171 (2020) 105370. https://doi.org/https://doi.org/10.1016/j.ijmecsci.2019.105370.

[18] C.-M. Sanchez-Camargo, A. Hor, M. Salem, C. Mabru, A robust method for mechanical characterization of heterogeneous materials by nanoindentation grid analysis, Mater. Des. 194 (2020) 108908. https://doi.org/https://doi.org/10.1016/j.matdes.2020.108908.

[19] W. Liu, J. Lian, N. Aravas, S. Münstermann, A strategy for synthetic microstructure generation and crystal plasticity parameter calibration of fine-grain-structured dual-phase steel, Int. J. Plast. 126 (2020) 102614. https://doi.org/https://doi.org/10.1016/j.ijplas.2019.10.002.

[20] A.F. Gerday, M. Ben Bettaieb, L. Duchene, N. Clement, H. Diarra, A.M. Habraken, Interests and limitations of nanoindentation for bulk multiphase material identification: Application to the beta phase of Ti-5553, Acta Mater. 57 (2009) 5186–5195. http://www.sciencedirect.com/science/article/pii/S1359645409004431.

[21] A.F. Gerday, M. Ben Bettaieb, L. Duchêne, N. Clement, H. Diarra, A.M. Habraken, Material behavior of the hexagonal alpha phase of a titanium alloy identified from nanoindentation tests, Eur. J. Mech. - A/Solids. 30 (2011) 248–255. https://doi.org/https://doi.org/10.1016/j.euromechsol.2010.11.001.

[22] C. Rojas-Ulloa, C. Bouffioux, A.F. Jaramillo, C.M. García-Herrera, T. Hussain, L. Duchêne, G. Riu, J. Josep Roa, P. Flores, A. Marie Habraken, V. Tuninetti, Nanomechanical characterization of the deformation response of orthotropic Ti–6Al–4V, Adv. Eng. Mater. (2021) 2001341. https://doi.org/https://doi.org/10.1002/adem.202001341.

[23] O. Dedry, C. Bouffioux, H. S. Tran, J.G.S. Macias, A.M. Habraken, A. Mertens, Identification of AlSi10Mg matrix behavior by nanoindentation, in: Proc. 24th Int. ESAFORM Conf. Mater. Form., 2021.

https://popups.uliege.be/esaform21/index.php?id=2464.

[24] C.A. Schuh, Nanoindentation studies of materials, Mater. Today. 9 (2006). https://doi.org/10.1016/S1369-7021(06)71495-X.

[25] T. Nakamura, Y. Gu, Identification of elastic-plastic anisotropic parameters using instrumented indentation and inverse analysis, Mech. Mater. 39 (2007) 340–356. http://www.sciencedirect.com/science/article/pii/S0167663606000718.

[26] E. Renner, A. Bourceret, Y. Gaillard, F. Amiot, P. Delobelle, F. Richard, Identifiability of single crystal plasticity parameters from residual topographies in Berkovich nanoindentation on FCC nickel, J. Mech. Phys. Solids. 138 (2020) 103916. https://doi.org/https://doi.org/10.1016/j.jmps.2020.103916.

[27] C. Heinrich, A.M. Waas, A.S. Wineman, Determination of material properties using nanoindentation and multiple indenter tips, Int. J. Solids Struct. 46 (2009) 364–376. http://www.sciencedirect.com/science/article/pii/S0020768308003612.

[28] S. Basu, A. Moseson, M.W. Barsoum, On the determination of spherical nanoindentation stress-strain curves, J. Mater. Res. 21 (2006). https://doi.org/10.1557/jmr.2006.0324.

[29] S.W. Moore, M.T. Manzari, Y.-L. Shen, Nanoindentation in elastoplastic materials: insights from numerical simulations, Int. J. Smart Nano Mater. 1 (2010) 95–114. https://doi.org/10.1080/19475411003589889.

[30] H. Pelletier, J. Krier, P. Mille, Characterization of mechanical properties of thin films using nanoindentation test, Mech. Mater. 38 (2006) 1182–1198. http://www.sciencedirect.com/science/article/pii/S0167663606000196.

[31] Y. Liu, X. Zhao, D. Wang, Determination of the plastic properties of materials treated by ultrasonic surface rolling process through instrumented indentation, Mater. Sci. Eng. A. 600 (2014) 21–31. https://doi.org/https://doi.org/10.1016/j.msea.2014.01.096.

[32] G. Cheng, K.S. Choi, X. Hu, X. Sun, Determining individual phase properties in a multi-phase Q&P steel using multi-scale indentation tests, Mater. Sci. Eng. A. 652 (2016) 384–395. http://www.sciencedirect.com/science/article/pii/S0921509315306596.

[33] E. Harsono, S. Swaddiwudhipong, Z.S. Liu, L. Shen, Numerical and experimental indentation tests considering size effects, Int. J. Solids Struct. 48 (2011) 972–978. https://doi.org/https://doi.org/10.1016/j.ijsolstr.2010.12.002.

[34] G. Constantinides, K.S. Ravi Chandran, F.J. Ulm, K.J. Van Vliet, Grid indentation analysis of composite microstructure and mechanics: Principles and validation, Mater. Sci. Eng. A. 430 (2006) 189–202. http://www.sciencedirect.com/science/article/pii/S0921509306009294.

[35] B. Bhushan, X. Li, Nanomechanical characterisation of solid surfaces and thin films, Int. Mater. Rev. 48 (2003) 125–164. https://doi.org/10.1179/095066003225010227.

[36] N.X. Randall, M. Vandamme, F.J. Ulm, Nanoindentation analysis as a two-dimensional tool for mapping the mechanical properties of complex surfaces, 2011/01/31 (2009) 679–690. https://www.cambridge.org/core/article/nanoindentation-analysis-as-a-twodimensional-tool-for-mapping-the-mechanical-properties-of-complex-surfaces/2A778ECC26E6F04DE80ACD81DF1F259B.

[37] X. Chen, I.A. Ashcroft, R.D. Wildman, C.J. Tuck, A combined inverse finite element – elastoplastic modelling method to simulate the size-effect in nanoindentation and characterise materials from the nano to micro-scale, Int. J. Solids Struct. 104–105 (2017) 25–34. https://doi.org/https://doi.org/10.1016/j.ijsolstr.2016.11.004.

[38] X. Chen, I.A. Ashcroft, C.J. Tuck, Y.F. He, R.J.M. Hague, R.D. Wildman, An investigation into the depth and time dependent behavior of UV cured 3D ink jet printed objects, J. Mater. Res. 32 (2017) 1407–1420. https://doi.org/10.1557/jmr.2017.4.

[39] M. Liu, C. Lu, K. Tieu, H. Yu, Numerical comparison between Berkovich and conical nano-indentations: Mechanical behaviour and micro-texture evolution, Mater. Sci. Eng. A. 619 (2014) 57–65. https://doi.org/https://doi.org/10.1016/j.msea.2014.09.034.

[40] M. Liu, C. Lu, K.A. Tieu, C.-T. Peng, C. Kong, A combined experimental-numerical approach for determining mechanical properties of aluminum subjects to nanoindentation, Sci. Rep. 5 (2015) 15072. https://doi.org/10.1038/srep15072.

[41] J.L. Bucaille, A. Rossoll, B. Moser, S. Stauss, J. Michler, Determination of the matrix in situ flow stress of a continuous fibre reinforced metal matrix composite using instrumented indentation, Mater. Sci. Eng. A. 369 (2004) 82–92. https://doi.org/https://doi.org/10.1016/j.msea.2003.10.288.

[42] J.L. Bucaille, S. Stauss, P. Schwaller, J. Michler, A new technique to determine the elastoplastic properties of thin metallic films using sharp indenters, Thin Solid Films. 447–448 (2004) 239–245. http://www.sciencedirect.com/science/article/pii/S0040609003011003.

[43] A.G. Atkins, D. Tabor, Plastic indentation in metals with cones, J. Mech. Phys. Solids. 13 (1965) 149–164. https://doi.org/https://doi.org/10.1016/0022-5096(65)90018-9.

[44] D. Tabor, Indentation hardness: Fifty years on a personal view, Philos. Mag. A. 74 (1996) 1207–1212. https://doi.org/10.1080/01418619608239720.

[45] I.M. Hutchings, The contributions of David Tabor to the science of indentation hardness, J. Mater. Res. 24 (2009) 581–589. https://doi.org/10.1557/jmr.2009.0085.

[46] Y.-T. Cheng, C.-M. Cheng, Scaling approach to conical indentation in elastic-plastic solids with work hardening, J. Appl. Phys. 84 (1998) 1284–1291. https://doi.org/10.1063/1.368196.

[47] M. Dao, N. Chollacoop, K.J. Van Vliet, T.A. Venkatesh, S. Suresh, Computational modeling of the forward and reverse problems in instrumented sharp indentation,

Acta Mater. 49 (2001) 3899–3918. https://doi.org/https://doi.org/10.1016/S1359-6454(01)00295-6.

[48] N. Ogasawara, N. Chiba, X. Chen, Representative strain of indentation analysis, J. Mater. Res. 20 (2005) 2225–2234. https://doi.org/10.1557/JMR.2005.0280.

[49] J.L. Bucaille, S. Stauss, E. Felder, J. Michler, Determination of plastic properties of metals by instrumented indentation using different sharp indenters, Acta Mater. 51 (2003) 1663–1678. http://www.sciencedirect.com/science/article/pii/S1359645402005682.

[50] K.K. Tho, S. Swaddiwudhipong, Z.S. Liu, K. Zeng, Simulation of instrumented indentation and material characterization, Mater. Sci. Eng. A. 390 (2005) 202–209. https://doi.org/https://doi.org/10.1016/j.msea.2004.08.037.

[51] S. Swaddiwudhipong, K.K. Tho, Z.S. Liu, K. Zeng, Material characterization based on dual indenters, Int. J. Solids Struct. 42 (2005) 69–83. https://doi.org/https://doi.org/10.1016/j.ijsolstr.2004.07.027.

[52] F. Han, B. Tang, X. Yan, Y. Peng, H. Kou, J. Li, Y. Deng, Y. Feng, Indentation pileup behavior of Ti-6Al-4V alloy: Experiments and nonlocal crystal plasticity finite element simulations, Metall. Mater. Trans. A. 48 (2017) 2051–2061. https://doi.org/10.1007/s11661-016-3946-0.

[53] J. Cheng, R. Lane, M.S. Kesler, J. Brechtl, X. Hu, R. Mirzaeifar, O. Rios, A.M. Momen, K. Nawaz, Experiment and non-local crystal plasticity finite element study of nanoindentation on Al-8Ce-10Mg alloy, Int. J. Solids Struct. 233 (2021) 111233. https://doi.org/https://doi.org/10.1016/j.ijsolstr.2021.111233.

[54] A. Greco, E. Sgambitterra, F. Furgiuele, A new methodology for measuring residual stress using a modified Berkovich nano-indenter, Int. J. Mech. Sci. 207 (2021) 106662. https://doi.org/https://doi.org/10.1016/j.ijmecsci.2021.106662.

[55] R. Moharrami, M. Sanayei, Improvement of indentation technique for measuring general biaxial residual stresses in austenitic steels, Precis. Eng. 64 (2020) 220–227.

https://doi.org/https://doi.org/10.1016/j.precisioneng.2020.04.011.

[56] Y.-L. Shen, J.J. Williams, G. Piotrowski, N. Chawla, Y.L. Guo, Correlation between tensile and indentation behavior of particle-reinforced metal matrix composites: an experimental and numerical study, Acta Mater. 49 (2001) 3219–3229. https://doi.org/https://doi.org/10.1016/S1359-6454(01)00226-9.

[57] Y.-L. Shen, Y.L. Guo, Indentation modelling of heterogeneous materials, Model. Simul. Mater. Sci. Eng. 9 (2001) 391–398. https://doi.org/10.1088/0965-0393/9/5/304.

[58] R. Ekici, M. Kemal Apalak, M. Yıldırım, F. Nair, Effects of random particle dispersion and size on the indentation behavior of SiC particle reinforced metal matrix composites, Mater. Des. 31 (2010) 2818–2833. https://doi.org/https://doi.org/10.1016/j.matdes.2010.01.001.

[59] F. Pöhl, S. Huth, W. Theisen, Finite element method-assisted acquisition of the matrix influence on the indentation results of an embedded hard phase, Mater. Sci. Eng. A. 559 (2013) 822–828. https://doi.org/https://doi.org/10.1016/j.msea.2012.09.029.

[60] K. Durst, M. Göken, H. Vehoff, Finite element study for nanoindentation measurements on two-phase materials, J. Mater. Res. 19 (2004) 85–93. https://doi.org/DOI: 10.1557/jmr.2004.19.1.85.

[61] P. Duan, Y. Xia, S. Bull, J. Chen, Finite element modeling of nanoindentation response of elastic fiber-matrix composites, J. Mater. Res. 33 (2018) 2494–2503. https://doi.org/10.1557/jmr.2018.243.

[62] X. Xiao, D. Terentyev, A. Ruiz, A. Zinovev, A. Bakaev, E.E. Zhurkin, High temperature nano-indentation of tungsten: Modelling and experimental validation, Mater. Sci. Eng. A. 743 (2019) 106–113. https://doi.org/https://doi.org/10.1016/j.msea.2018.11.079.

[63] O. Casals, J. Očenášek, J. Alcalá, Crystal plasticity finite element simulations of

pyramidal indentation in copper single crystals, Acta Mater. 55 (2007) 55–68. https://doi.org/https://doi.org/10.1016/j.actamat.2006.07.018.

[64] C. Zambaldi, Y. Yang, T.R. Bieler, D. Raabe, Orientation informed nanoindentation of alpha-titanium: Indentation pileup in hexagonal metals deforming by prismatic slip, J. Mater. Res. 27 (2012) 356–367.

[65] M. Toparli, N.S. Koksal, Hardness and yield strength of dentin from simulated nano-indentation tests, Comput. Methods Programs Biomed. 77 (2005) 253–257. https://doi.org/https://doi.org/10.1016/j.cmpb.2004.11.003.

[66] L.M. Farrissey, P.E. McHugh, Determination of elastic and plastic material properties using indentation: Development of method and application to a thin surface coating, Mater. Sci. Eng. A. 399 (2005) 254–266. https://doi.org/https://doi.org/10.1016/j.msea.2005.03.109.

[67] M. Khelifa, V. Fierro, A. Celzard, Finite element simulation of nanoindentation tests using a macroscopic computational model, J. Mech. Sci. Technol. 28 (2014) 3209–3217. https://doi.org/10.1007/s12206-014-0730-1.

[68] G. Sun, E. Wang, T. Zhao, G. Zheng, Q. Li, Inverse identification of cell-wall material properties of closed-cell aluminum foams based upon Vickers nano-indentation tests, Int. J. Mech. Sci. 176 (2020) 105524. https://doi.org/https://doi.org/10.1016/j.ijmecsci.2020.105524.

[69] M.K. Khan, S. V Hainsworth, M.E. Fitzpatrick, L. Edwards, A combined experimental and finite element approach for determining mechanical properties of aluminium alloys by nanoindentation, Comput. Mater. Sci. 49 (2010) 751–760. https://doi.org/https://doi.org/10.1016/j.commatsci.2010.06.018.

[70] Y.-T. Cheng, C.-M. Cheng, Scaling, dimensional analysis, and indentation measurements, Mater. Sci. Eng. R Reports. 44 (2004) 91–149. https://doi.org/https://doi.org/10.1016/j.mser.2004.05.001.

[71] J.G. Santos Macias, C. Elangeswaran, L. Zhao, B. Van Hooreweder, J.. Adrien, E.

Maire, J.Y. Buffiiere, W. Ludwig, P.J. Jacques, A. Simar, Ductilisation and fatigue life enhancement of selective laser melted AlSi10Mg by friction stir processing, Scr. Mater. 170 (2019) 124–128. http://www.sciencedirect.com/science/article/pii/S135964621930332X.

[72] I.N. Sneddon, The relation between load and penetration in the axisymmetric boussinesq problem for a punch of arbitrary profile, Int. J. Eng. Sci. 3 (1965) 47–57. https://doi.org/https://doi.org/10.1016/0020-7225(65)90019-4.

[73] J.G. Santos Macías, T. Douillard, L. Zhao, E. Maire, G. Pyka, A. Simar, Influence on microstructure, strength and ductility of build platform temperature during laser powder bed fusion of AlSi10Mg, Acta Mater. 201 (2020) 231–243. https://doi.org/https://doi.org/10.1016/j.actamat.2020.10.001.

[74] C.F. Guzman, J. Gu, J. Duflou, H. Vanhove, P. Flores, A.M. Habraken, Study of the geometrical inaccuracy on a SPIF two-slope pyramid by finite element simulations, Int. J. Solids Struct. 49 (2012) 3594–3604. http://www.sciencedirect.com/science/article/pii/S0020768312003010.

[75] L. Duchêne, P. de Montleau, A.M. Habraken, Development and performance assessment of an improved 8-node mixed type FEM element, in: P.A. Edited by N. Juster and A. Rosochowski. Krakow (Ed.), Proc. 9th Int. ESAFORM Conf. Mater. Forming., 2006: pp. 135–138. http://hdl.handle.net/2268/11534.

[76] J.I. V de Sena, C.F. Guzmán, L. Duchêne, A.M. Habraken, A.K. Behera, J. Duflou, R.A.F. Valente, R.J.A. de Sousa, Simulation of a two-slope pyramid made by SPIF using an adaptive remeshing method with solid-shell finite element, Int. J. Mater. Form. 9 (2016) 383–394. https://doi.org/10.1007/s12289-014-1213-8.

[77] A.M. Habraken, S. Cescotto, Contact between deformable solids: The fully coupled approach, Math. Comput. Model. 28 (1998) 153–169. https://doi.org/https://doi.org/10.1016/S0895-7177(98)00115-0.

[78] T.H. Wang, T.-H. Fang, Y.-C. Lin, A numerical study of factors affecting the

characterization of nanoindentation on silicon, Mater. Sci. Eng. A. 447 (2007) 244–253. https://doi.org/https://doi.org/10.1016/j.msea.2006.10.077.

[79] J. Nafar Dastgerdi, B. Anbarlooie, S. Marzban, G. Marquis, Mechanical and real microstructure behavior analysis of particulate-reinforced nanocomposite considering debonding damage based on cohesive finite element method, Compos. Struct. 122 (2015) 518–525. https://doi.org/10.1016/j.compstruct.2014.12.009.

[80] S. Ma, X. Zhuang, X. Wang, 3D micromechanical simulation of the mechanical behavior of an in-situ Al3Ti/A356 composite, Compos. Part B Eng. 176 (2019) 107115. https://doi.org/https://doi.org/10.1016/j.compositesb.2019.107115.

[81] X. Gao, X. Zhang, M. Qian, L. Geng, Effect of reinforcement shape on fracture behaviour of SiC/Al composites with network architecture, Compos. Struct. 215 (2019) 411–420. https://doi.org/https://doi.org/10.1016/j.compstruct.2019.02.067.

[82] J.F. Zhang, X.X. Zhang, Q.Z. Wang, B.L. Xiao, Z.Y. Ma, Simulations of deformation and damage processes of SiCp/Al composites during tension, J. Mater. Sci. Technol. 34 (2018) 627–634. https://doi.org/https://doi.org/10.1016/j.jmst.2017.09.005.